Article:
Nerl, HC, Pokle, A, Jones, L et al. (15 more authors) (2019) Self-Assembly of Atomically Thin Chiral Copper Heterostructures Templated by Black Phosphorus. Advanced Functional Materials, 29 (37). 1903120. ISSN 1616-301X

https://doi.org/10.1002/adfm.201903120

Self-assembly of atomically-thin chiral Copper heterostructures templated by Black Phosphorus

*Hannah C. Nerl[1,2], Anuj Pokle, [1,3], Lewys Jones[1,3], Knut Müller-Caspary,[4] Karel H.W. van den Bos[4],Clive Downing,[3] Eoin K. McCarthy[3], Nicolas Gauquelin,[4] Quentin M. Ramasse[5,6,7] , Ivan Lobato,[4] Dermot Daly,[3] Juan Carlos Idrobo[8], *Sandra Van Aert,[4] Gustaaf Van Tendeloo,[4] Stefano Sanvito,[1,2] Jonathan N. Coleman,[1,2] *Clotilde S. Cucinotta,[9] and *Valeria Nicolosi [2,3,10]*

*Correspondence to: hcnerl@fhi-berlin.mpg.de; sandra.vanaert@uantwerpen.be; c.cucinotta@imperial.ac.uk; nicolov@tcd.ie

[1] School of Physics, Trinity College Dublin, Dublin 2, Ireland
[2] CRANN & AMBER, Trinity College Dublin, Dublin 2, Ireland
[3] Advanced Microscopy Laboratory, CRANN, Trinity College Dublin, Dublin 2, Ireland
[4] EMAT – University of Antwerp, Groenenborgerlaan 171, B-2020 Antwerp, Belgium
[5] SuperSTEM Laboratory, SciTech Daresbury Campus, Daresbury, WA4 4AD, UK
[6]School of Physics and [7]School of Chemical and Process Engineering, University of Leeds, Leeds LS2 9JT, UK
[8] Center for Nanophase Materials Sciences, Oak Ridge National Laboratory, Oak Ridge, TN 37831 USA
[9]TYC and Department of Chemistry, Imperial College London, UK
[10]School of Chemistry, Trinity College Dublin, Dublin 2, Ireland

Keywords: heterostructures, black phosphorus, self-assembly, chiral, 2D materials, nanostructures

The fabrication of two-dimensional systems for electronic devices is not straightforward with top-down low-yield methods often employed leading to irregular nanostructures and lower quality devices. Here a simple and reproducible method to trigger self-assembly of arrays of high aspect-ratio chiral copper heterostructures templated by the structural anisotropy in black phosphorus nanosheets will be presented. Using quantitative atomic resolution aberration-corrected scanning transmission electron microscopy imaging, *in-situ* heating transmission electron microscopy and electron energy-loss spectroscopy arrays of heterostructures forming at speeds exceeding 100 nm/s and displaying long-range order over microns were observed. The controlled instigation of the self-assembly of the Cu heterostructures embedded in BP was achieved using conventional electron beam lithography combined with site specific placement of Cu nanoparticles. Density functional theory calculations were used to

investigate the atomic structure and suggest a metallic nature of the Cu heterostructures grown in BP. The findings of this new hybrid material with unique dimensionality, chirality and metallic nature and its triggered self-assembly open new and exciting opportunities for next generation, self-assembling devices.

1. Introduction

Unlike graphene, semiconductor few-layer black phosphorus (BP) exhibits a direct bandgap[1] leading to diverse electronic and thermal properties[2-12]. BP was first successfully synthesised under pressure over a century ago[13]. However, only has the recent successful exfoliation of monolayer BP [2, 4, 14-15] led to its rediscovery for applications ranging from electronics, catalysis, sensors to biomedical drug delivery [16-34]. The structural anisotropy of BP leads to anisotropy in the transport properties and therefore to additional unique opportunities for applications [6, 8, 12, 35-36].

For many of these applications, there is a need for hybrid structures to combine the merits of low-dimensional materials for the design and fabrication of nanodevices by balancing requirements for electronic/electrical properties, improved stability and optical tenability. Multiple 2D materials, including BP, can be stacked vertically or stitched together to form in-plane heterojunctions, which combine the characteristics of the constituent compounds, thus allowing the tuning of electrical as well as optical properties [16-34, 37]. Another example of BP hybrid structures has been achieved by placing carbon nanotubes [38-39] on top of BP to combine their properties. However, in general, Van der Waals heterostructures grow with a variable interlayer distance and twist angles between the layers [11, 12] two features that are almost impossible to control. This makes their properties varying from sample to sample and the design of composite nanostructures becomes unpredictable and, in the worst case, unreliable. Furthermore, in order to preserve the properties of the individual materials in the heterojunctions, the fabrication of atomically sharp interfaces is crucial. This, however, can be extremely challenging. Even though attempts to synthesize lateral interfaces have been made,

roughness due to interfacial steps and traces of unwanted substitutional doping across the heterojunctions often result in a dilution or obliteration of the properties of the materials [13]–[16].

Here we propose a new hybrid nanostructure growth strategy. Our approach avoids the issues described above and uses a two-dimensional material to template the growth of novel hybrid structures.

This strategy is demonstrated here for the first time with BP, which is used to guide the self-assembly of highly directional Cu heterostructures templated by the underlying lattice structure. Our work uses atomic-resolution quantitative aberration-corrected scanning transmission electron microscopy (AC-STEM) imaging combined with simultaneous electron energy-loss spectroscopy (EELS) to demonstrate the *in situ* self-assembly of Cu heterostructures in a BP nanosheet matrix. Using density functional theory (DFT) calculations we studied the thermodynamic stability and growth of the Cu heterostructures and investigated their electronic structure.

2. Results and Discussion

2.1. Rapid in situ formation of Cu structures templated by BP lattice

High-angle annular dark field (HAADF) STEM imaging in **figure 1a** shows the self-assembled high-aspect-ratio Cu structures as they formed through the contact of Cu nanoparticles dropped onto the BP nanosheets. The same growth mechanism was observed for both liquid exfoliated as well as mechanically exfoliated BP nanosheets.

The synthesis of the hybrid material did not involve any surface treatment of the BP[40] or addition of surfactants[15] or C60 molecules[41] to improve the reduced stability of BP. This is an advantage of the self-assembly technique described here since it reduces not only steps in the synthesis process but it also keeps the BP surface structure as close as possible to that of BP nanosheets alone. However, the downside of keeping the BP surface intact and free of added molecules is that the stability in air of the hybrid material is comparable to that of BP

nanosheets.[15, 42-43] Therefore the material was therefore kept under vacuum conditions during the synthesis of BP and the self-assembly of the Cu structures. The Cu structure formation was studied using *in situ* heating transmission electron microscopy (TEM) and it was found that when heated to 300 ˚C, arrays of the structures as shown in figure 1b form rapidly. The growth speed was observed to exceed 100 nm/sec (structures grew across the whole field of view within the minimum microscope acquisition time). More details on the different stages of the heating experiment and the video showing the formation of the structures is shown in the supplementary information (**SI**), section **SI1** and **Movie S1** respectively. We expect the formation energy of these structures to strongly favour self-assembly as the BP was found to be an especially effective scavenger of any local Cu in the surroundings; this includes the self-formation using the Cu from the TEM support grid itself when heated even in the absence of specific Cu nanoparticle addition (also shown in SI). In all cases, the growth of the structures solely occurred along the [010] direction, as shown in the images in figure 1a&b. No growth was ever observed in any other direction. This strongly suggests that the Cu growth is templated by the lattice of the BP. The schematic of a BP nanosheet as seen along the [001] crystallographic direction shown in figure 1c illustrates the direction of the Cu structure growth (see **SI**, section **SI2** for more details on the BP lattice structure). In BP the P atoms join together to form a two-dimensional puckered sheet with natural channels along the [010] direction, forming adjacent hexagonal chairs in an orthorhombic arrangement [24]–[26]. A computational investigation showed the Cu atoms diffusing with a low energy barrier (ΔE = 0.14 eV) along the grooves of the BP lattice along the [010] direction (details in **SI**, section **SI5** for details on computational simulations), which further supports that the Cu growth is templated by the BP lattice.

2.2. Controlled initiation of self-assembly of Cu structures

Here we describe two techniques to successfully achieve a controlled seeding of Cu in the BP. In the first approach, Cu NPs were individually transferred using a micro-mechanical

manipulator onto a mechanically exfoliated BP flake already deposited on a silicon wafer. Cu atom diffusion was then achieved by simply heating the system. The second and more controllable technique involved using electron beam lithography to directly evaporate Cu to specific sites on the exfoliated BP nanosheets, already deposited on a silicon substrate. Heating to 300 ˚C enabled Cu diffusion. With both techniques, we achieved control over the growth initiation sites as the growth was observed originating solely from the BP nanosheet areas where the Cu NPs had been deposited. More details on these methods can be found in the **SI**, section **SI3**.

2.3. Polymorph, chiral Cu structures with unique dimensionality

Imaging of the structures grown in the BP is displayed in figure 1b,d&e where various structures in a multi-layered BP nanosheet are shown in the simultaneous dark field (DF) and bright field (BF) images (figure 1d and figure 1e respectively). The high-resolution images figure 1d&e show that the pair of structures to the left-hand-side of the images appears to undulate in a regular manner but the individual structure on the right-hand side appears to be straighter in comparison. The undulations have been found to follow a regular pattern with ~2nm periodicity (see **SI**, section **SI4** for more details).

Atomic resolution imaging of BP in both the [001] and R17/-R17 (tilted by 17° from [001], with R17 and -R17 being of opposite tilt direction and equivalent by symmetry in BP as described in the SI, section SI2) revealed that the Cu structures are only 3-atoms-wide (as shown in **figure 2a-e** and **figure 2f-h** respectively). The interaction of Cu with phosphorus was found to be highly localized (figure 2a and section SI 5). Core-loss electron energy-loss spectroscopy (EELS) (figure 2b-d) confirmed both that the structures are composed of Cu and that the separation between the Cu structures and the BP nanosheets is atomically sharp.

The structures also appear to be regularly spaced along [100] direction (in the direction perpendicular to the growth direction) as shown in figure 2g. This spacing was found to be multiples of 0.45nm, which matches the theoretically calculated distance between the grooves

in the [010] direction of the BP lattice (more details on the undulations as well as the spacing between structures can be found the SI, section SI4), again confirming that the growth is templated by the anisotropic geometry of the BP lattice.

DFT calculations showed that the diffusion of a Cu atom on a BP surface occurs interstitially, through a zigzag pathway joining the centres of the adjacent BP hexagonal chairs. Furthermore we found that the process leading to the formation of a Cu surface structure becomes more energetically favourable with increasing nanostructure length, which provides further computational support for the great speed of the structure formation we observed experimentally (for more details on the energetics and kinetics of Cu interaction with BP see **SI**, section **SI5**). Hence, the BP sheets provide the template for the Cu growth as shown by the combined evidence described above.

The undulations of the structure were clearly visible in atomic resolution images as shown in the STEM images in figure 2. In the thinner BP sheets, the Cu structures even exhibited undulations in the R17/-R17 orientation (figure 2f). The undulating pattern of the structures was found to vary in directionality across the structures. Structures 1&2 shown in figure 2h as well as structure 4 (which exhibits only very slight undulations) are of different chirality compared to structure 3. The structures also appear to introduce different steps into the different projections of the BP structure of the same thickness: structures 1-3 introduce a step, but structure 4 does not appear to do so (marked with a red dotted line in figure 2h). The same step difference was observed in the R17/-R17 orientation as shown in figure 2e. In both regions, the BP sheet adjacent to the Cu structures exhibits the same STEM intensity which indicates that the thickness is approximately constant (a quantitative STEM analysis will be presented below). This suggests that the observed difference in stepping behaviour is not a result of differing BP thicknesses. The observed differences in undulating patterns and step introduction could however result from different horizontal stacking of structures of different chirality and/or vertical offset between structures as well as from different Cu thicknesses or a

combination of all. Occasionally, Cu structures that terminate in the BP sheet were observed (shown in SI). This further supports the suggestion that the Cu structures are indeed heterostructures of a certain thickness which appear to vary in thickness between different structures.

However, in order to confirm the thickness of the Cu structures as well as to study their physical properties and formation process, a structure model of the arrangement of Cu and P atoms within one period of undulation is needed. First, we developed an empirical structure model to provide information on the projected Cu structures by comparing image simulations quantitatively with calibrated experimental STEM images. In a second step, we employed comprehensive DFT simulations to discuss the physical properties for a catalogue of closest-match Cu structures.

2.4. Wire versus heterostructure: thickness determination using quantitative imaging

HAADF STEM image-contrast quantification performed over a Cu//BP flake in its R17/-R17 direction was employed to study the precise thicknesses (the height of the structures in the EM projections) by quantitatively comparing experiment with simulations. [44-45]

Since the structure of the BP is well known, the comparison of thickness-dependent STEM intensity simulations with calibrated experimental images allows for the accurate measurement of the sheet thickness in regions of pure BP. The average BP sheet thickness in the region shown in **figure 3a** was measured to be 5.5 nm in the R17/-R17 orientation, the equivalent of 9 BP unit cells. This knowledge of the exact BP thickness was then employed to develop an empirical structure model for the Cu structure to consistently account for the relative contrast in the Cu sites compared to the BP sites. On first assessment, the significant additional contrast in the Cu sites compared to the BP sites in a nanosheet of 5.5nm thickness cannot be explained by the addition of an individual Cu nanowire. Hence experimental and computational evidence strongly suggests that the Cu structures forming in the BP are in fact 2D heterostructures. In order to confirm this hypothesis, the knowledge of the exact BP

thickness and the periodicity of the Cu structure assessed by template matching (image shown in figure 3c) were used to develop the empirical model structure for the Cu heterostructure shown in figure 3b. The validity of this empirical model structure was assessed using dynamical multi-slice simulations with the MULTEM software [46] to obtain the simulated image shown in figure 3d which shows a close match to experiment in the R17/-R17 projection. The close match between the relative contrast in the electron microscopy projections and the image simulated from the empirical model structure suggests that the Cu structure is indeed a 2D heterostructure and not an individual nanowire of Cu. Experimentally, the Cu heterostructures were observed in BP for thicknesses from ~5 or more unit cells only. These 2D heterostructures are most likely composed of stacks of structures that interact with each other to form regular but chiral polymorph 2D heterostructures of Cu in the BP nanosheets composed of several layers of BP.

Armed with this knowledge we proceeded using density functional theory (DFT) calculations to study the nanoscopic, atomic and electronic structure of the Cu heterostructures.

2.5. Theoretical investigation of chiral polymorphism and metallic nature

The chiral polymorphism of the observed experimental structure was confirmed by our DFT calculations which showed different metastable chiral polymorphs of width ranging from 0.365 nm to 0.375 nm, depending on the structure. We then simulated images using the calculated DFT structures to directly compare them to experimental electron micrographs (using the fast image simulation tool Prismatic STEM [46] see methods section for details of the simulation parameters).

The Cu heterostructure that most closely matched the experiment was also one of the computationally most stable, with a formation energy of 0.60 eV/Cu atom (T-S-3 structure in **SI**, **section SI5**). As observed in the experimental *in situ* measurements, the DFT 2D heterostructure also forms along the natural BP growth channel in the [010] direction and extends transversally along the [001] direction. The DFT heterostructure results from the

vertical alignment of three-atoms-wide Cu wires with a triangular cross section, growing interstitially within BP layers as shown in **Figure 4.a**. Wires belonging to adjacent BP layers grow with an offset of one BP lattice parameter along the [010] direction, such that the heterostructure, appears continuous along the growth path, when observed along the [001] direction, while gaps are exposed when the structure is rotated by 17˚ (or by -17 ˚depending on the chirality of the heterostructure).

As described earlier, R17 and –R17 orientations of clean BP are equivalent by symmetry, but the chiral nature of the Cu heterostructures investigated causes this symmetry to be broken. Without knowledge of the exact 3D structure there is no way to distinguish between both orientations experimentally. However, it is possible to observe the DFT structures from different orientations and compare the simulated EM projections of the DFT structure in the R17 and -R17 orientations. When doing so, it becomes evident that the simulated images of the same chiral structure in the R17 and -R17 orientations are indeed distinct (as shown in Figure 4.a-b, additional image simulations of all orientations can be found in the SI, Figure S14 and Figure S15).

The simulated images of the T-S-3 structure are shown in Figure 4.b, in i) [001] and iii) -R17 orientations respectively. The corresponding experimental electron micrographs are shown in ii) and iv) respectively. Several different polymorphs of the T-S-3 structure were computationally observed, mainly differing for the chirality of the structure and the disposition and/or density of the atoms along the central axis of Cu heterostructure. The formation energies of such polymorphs are very similar, and range from 0.6 to 0.7 eV/Cu atom (see **SI**, section **SI6:** T structures in **SI Table S1**).

To computationally confirm that the Cu structure is indeed a 2D heterostructure and not an individual Cu nanowire, we separately simulated the isolated nanowire intercalated within the BP, and found out that, although thermodynamically viable, its formation within BP

(formation energy of ~0.27 eV/Cu atom) is less favorable than the formation of the 2D nanostructure.

In addition, both the same undulations in the simulated images as observed experimentally, and the continuity of the Cu heterostructure as observed from [001] direction are fully recovered only when relaxing the replicated nanowire unit to form the heterostructure (SI, Figure S14 and Figure S15).

Furthermore, we found that the image simulations of the EM projections of the DFT structure reproduce the step in the BP lattice in the –R17 but not in the R17 orientation as observed experimentally. These findings prove that the chiral nature of the Cu heterostructure is at the origin of the conformational variations observed experimentally.

Besides the most stable structure and its chiral polymorphs, our computational results show that a number of other metastable heterostructures can also be formed (with formation energies ranging from 0.5 to 0.2 eV/Cu atom), either composed by intercalated nanotubes with hexagonal cross-sections, or by nanowires with pentagonal or irregular cross-sections. The Cu atoms in these structures partially occupy substitutional positions, after a dissociative processes leading to the release of P atoms. (A full catalogue of 2D heterostructures and the corresponding image simulations can be found in the SI Table S1.)

The analysis of the density of states of the T-S-3 structure (see figure 4c) suggests that the heterostructure is metallic. This is proven by a densification of the density of states around the Fermi level of the decorated system, with Bloch states and charge density localized around the wire (see SI section SI5 for more details). This metallic character is present in all the metastable nanostructures observed computationally. An overlap of Cu and P centered states localized around the wire is also observed at all energies. As stated, because several other structures of similar formation energy could also form, there may be other electronic and structural variations of these wires.

3. Conclusion

Initiating the self-assembly of the metallic Cu heterostructures in situ in the BP nanosheets and thereby producing a hybrid material represents a novel way to fabricate nanodevices. Issues occurring during conventional fabrication of hybrid structures, including uncontrollable effects of stacking and relative orientation of materials, unwanted substitutional doping across heterostructures and interface roughness may thereby be elegantly avoided. Moreover, controlled seeding of Cu in BP was achieved with e-beam lithography, a standard technique used in the semiconducting industry which is readily scalable. Importantly, this can enable the use of existing technology and hardware to fabricate and design future BP-based electronic devices. The synthesis of the hybrid material did not involved any surface treatment of the BP[40] or addition of surfactants[15] or C60 molecules[41] to improve the reduced stability of BP. This is an advantage of the self-assembly technique described here since it reduces not only steps in the synthesis process but it also keeps the BP surface structure as close as possible to that of BP nanosheets alone. However, the downside of keeping the BP surface intact and free of added molecules is that the stability in air of the hybrid material is comparable to that of BP nanosheets.[15, 42-43] Therefore adding the metallic nature, unique dimensionality (few-atoms-wide and microns long) and chirality of the Cu heterostructures to the inherently promising properties of BP make this novel hybrid material of great interest for a whole range of potential applications in plasmonics, nanocatalysis, nanosensors, ICT and related areas. The very high aspect ratio of the Cu heterostructures in the BP nanosheets further increases the structural anisotropy already existing in BP nanosheets. This structural anisotropy in BP is at the root of very desirable, highly-directional optical, thermal and electrical properties in BP [2, 6, 8, 35-36] and these properties are expected to be further enhanced by the addition of the embedded metallic heterostructures and further studies of this are planned. Most importantly, the addition of chirality to the highly-directional properties inherent to BP allows for an additional degree of freedom when it comes to device fabrication which makes this intriguing novel hybrid material unique and of great interest for use in electronics.

4. Experimental Section

Samples: The black phosphorus was purchased from Smart Elements (Art. Nr. 003933), and crystals were stored in a glove box (MBraun) to avoid degradation (H_2O and O_2 levels below 0.1 ppm). The mechanical exfoliation was carried out using NITTO blue tape (BT-150E-CM) inside the glove box. Liquid-phase exfoliation was carried out using isopropyl alcohol (IPA) as a solvent and sonication using a sonic tip (Fisher Scientific) for 4 hrs at 60% amplitude.[47] The obtained dispersions were centrifuged in a Heraeus Multifuge X1 Centrifuge at 3000 rpm for 90 minutes, followed by the separation of the supernatant from the non-exfoliated material. The exfoliated sheets were deposited on TEM holey carbon 200 mesh Cu grids purchased from SPI Supplies. Initially the wire growth was achieved by thermally treating the TEM grids in a vacuum oven (2×10^{-3} mbar) kept at 110 °C for 5 days. The thermal treatment could also be achieved using a hot plate (IKA RCT basic) kept at 300 °C for 5 min.

Growth of Copper heterostructures: For the controlled growth study, we used two different approaches: First, we drop-cast Cu nanoparticles on an SEM stub and then lifted them by Coulomb interaction using a fine needle (Picoprobe - GGB Industries controlled by Kleindiek-nanotechnik) in a Carl Zeiss Auriga FIB, operated at 5 kV. This way we could transfer particles onto exfoliated BP flakes deposited atop a silicon wafer (University Wafer).

The second methodology involved first exfoliating the BP nanosheets and transferring them onto a silicon wafer, followed by lithography using a Raith beam blanking system on a Carl Zeiss Supra 40 SEM and then by e-beam metal evaporation using a Temescal. More details on both growth procedures can be found in the SI.

Microscopy: Scanning Electron Microscopy (SEM) images of the controlled growth study were acquired using a Carl Zeiss Ultra operated at 5 kV. Aberration-corrected STEM (AC-STEM) HAADF imaging and EELS were carried out in a NION UltraSTEM200, operated at 60 kV: for these experiments, the probe convergence semi-angle was 35 mrad with a probe

current of 35 pA, resulting in a probe size of 1.2 Å. Further imaging was carried out in a Nion UltraSTEM100MC 'Hermes', also operated at 60 kV: for these experiments, the probe convergence semi-angle was 31mrad with a probe current of 50 pA, resulting in a probe size of 1 Å. The HAADF detector inner and outer angles were calibrated as 85 mrad and 185 mrad respectively. Both microscopes are fitted with a Gatan Enfinium spectrometer for EELS. *In situ* heating measurements were performed on a S/TEM FEI TITAN 80-300, operated at 300 kV using a DENS wildfire holder. It is based on a Micro-Electro-Mechanical System (MEMS), controlling the temperature environment locally on the device by 4-point-probe. The temperature was initially varied from room temperature to 300 °C at 50 °C interval and kept at 300 °C for 65 min. The temperature was then raised to 500 °C with 50 °C interval. The mechanically exfoliated BP was placed over the MEMS electron transparent windows and Cu nanoparticles (Sigma Aldrich 774111-5G) were drop-cast over it.

Image processing: The HAADF STEM image shown figure 2b was frame averaged and the image shown in fig.3b was frame-averaged [48], then template-matched, then denoised.[48]

EELS processing: Digital Micrograph was used to perform the EELS and STEM analysis. Principal Component Analysis (Multivariate Statistical Analysis from the Interdisciplinary Centre for Electron Microscopy (CIME) using 60 components were used for de-noising the STEM EELS maps shown in fig.2.[49]

Density functional theory: The DFT approach was applied as implemented in the CP2K code (www.cp2k.org). The CP2K Kohn and Sham orbitals were expanded in a mixed Gaussian (double-ζ plus polarization, DZVP) and plane-waves basis set. A 600 Ryd energy cut-off was used for the plane-wave expansion of the electronic density. Tether and Goedecker-type pseudopotentials were used for all atoms, and Brillouin Zone integration was restricted to the Γ-point. The geometry and simulation cell were relaxed until the maximum force on each atom was less than 0.01 eV/Å. The PBE [50] exchange and correlation functional was used with

a Van der Waals correction at the Grimme-D3 level [51] The Nudged Elastic Band (NEB) approach in its climbing image implementation was used to evaluate energy barriers along the Cu diffusion pathway heterostructure [52-53]. Adsorption energies per Cu atom were evaluated as $\Delta E = (E_{BP} + nE_{Cu} - E_{Cu@BP} - n'E_P)/n$, where E_{BP} is the energy of the reference bulk BP slab, E_{Cu} is the chemical potential of a Cu atom (as taken from a reservoir represented by a 841 atoms Cu cluster), $E_{Cu@BP}$ is the energy of the decorated BP slab, *n* is the number of the adsorbed Cu atoms (N_{Cu} in table SI13 in SI) and *n'* the number of P atoms that have been released (P_{subst} in Table S1, in the SI). EP is the energy of a P atom, taken from a reservoir represented by the ideal BP bulk reference. More detail about the modelling of the interstitial periodical 2D heterostructures within BP is reported in SI.

Quantitative HAADF STEM: Quantitative STEM imaging was carried out at the FEI X-Ant-EM Titan class microscope at EMAT (Antwerp), which is equipped with an aberration corrector for the probe-forming system. The microscope was operated at 120keV primary energy and HAADF STEM images were acquired with a Fischione Model 3000 detector operated in its linear range, with acceptance angles of 46 to 215 mrad. Measured intensities were normalised to the incident beam intensity and compared to simulations employing the MULTEM software, which took the inhomogeneous detector sensitivity and partial spatial coherence into account. Thermal diffuse scattering was simulated with the frozen phonon model in an Einstein approximation using 20 phonon configurations. Statistical parameter estimation theory was employed as implemented in the StatSTEM software [34] to model the intensity distribution of each atomic column with a Gaussian in both simulation and experiment. This yields the integral scattered intensity of an atomic column, the scattering cross-section, which increases monotonically with specimen thickness. In order to improve the precision, we measured the cross-section of a P-dumbbell and compared with its simulated counterpart to determine the specimen thickness in Fig. 3a.

Further image simulations: Faster, less comprehensive image simulations of BP were performed using the Prismatic Software for STEM simulation.[54] Settings used: 1 frozen phonon per simulation for simulations shown in SI, 5 frozen phonons for the main paper (when directly comparing for the same structure, only slight improvements in noise-levels were observed when comparing images generated using between 1 up to 20 frozen phonons); potential bound = 0.3 Å; Pixel size = 0.1x0.1 Å. Images were generated for outer detector angles up to 200 mrad. A source size of 0.8 Å was added as well as a realistic noise level using a Matlab routine based on a Poisson distribution function.

Supporting Information

All supporting Information is available from the Wiley Online Library.

The following information can be found in the main SI file:

- SI 1 Ex-situ and In-situ Heating Experiments
- SI2 Orientations of Black Phosphorus
- SI3 Controlled instigation of self-assembly of Cu heterostructures
- SI4 Undulations of copper heterostructures and spacing between copper heterostructures in black phosphorus
- SI 5 Computational Approach and Modelling

In addition the following files are provided separately:

- Table S1. Catalogue showing the stable and energetically favorable 2D copper (Cu) heterostructures within black phosphorus (BP) bulk as found using an iterative combination of density functional theory (DFT) and image simulation (Prismatic).
- Movie S1. *In-situ* heating Transmission Electron Microscopy (TEM) of the growth process of the Cu heterostructures.

5. Acknowledgements

The authors acknowledge support from the European Research Council (ERC Starting Grant 2DNanoCaps, ERC TC2D, ERC CoG 3D2DPrint, ERC CoG Picometrics), FP7 ITN (MoWSeS), SFI (PIYRA and AMBER) and EPSRC (EP/P033555/1). Most of the imaging/analysis for this project was carried out at the Advanced Microscopy Laboratory (AML) at the AMBER centre, CRANN Institute www.tcd.ie/crann/aml/, Trinity College Dublin, Ireland. AML is an SFI supported imaging and analysis centre. K.M.-C., KH.W.v.d.B, I.L., N.G., S.V.A., and G.V.T. acknowledge support from the Research Foundation Flanders (FWO, Belgium) and the GOA project “Solarpaint" of the University of Antwerp. The Qu-Ant-EM microscope was partly funded by the Hercules fund from the Flemish Government.

JCI acknowledges support from the Center for Nanophase Materials Sciences, which is a DOE Office of Science User Facility. We thank Julia Kremer and Akshara Verma (CRANN, Trinity College Dublin) for their assistance using the Temescal. SuperSTEM is the U.K. National Research Facility for Advanced Electron Microscopy, supported by the Engineering and Physical Sciences Research Council (EPSRC). All the calculations were performed using the ARCHER, UK, National Supercomputing Service (http://www.archer.ac.uk, via our membership of the UK's HEC Materials Chemistry Consortium, which is funded by EPSRC (EP/R029431)), and the Kelvin and Boyle clusters, maintained by the Trinity Centre for High Performance Computing (project id: HPC_16_00932, these clusters were funded through grants from Science Foundation Ireland).

Author 1 and Author 2 contributed equally to this work.

Received: ((will be filled in by the editorial staff))

Revised: ((will be filled in by the editorial staff))

Published online: ((will be filled in by the editorial staff))

References

1. Castellanos-Gomez, A.; Vicarelli, L.; Prada, E.; Island, J. O.; Narasimha-Acharya, K. L.; Blanter, S. I.; Groenendijk, D. J.; Buscema, M.; Steele, G. A.; Alvarez, J. V.; Zandbergen, H. W.; Palacios, J. J.; van der Zant, H. S. J., Isolation and characterization of few-layer black phosphorus. *2d Mater* **2014,** *1* (2).
2. Xia, F.; Wang, H.; Jia, Y., Rediscovering black phosphorus as an anisotropic layered material for optoelectronics and electronics. *Nat Commun* **2014,** *5*, 4458.
3. Das, S.; Zhang, W.; Demarteau, M.; Hoffmann, A.; Dubey, M.; Roelofs, A., Tunable transport gap in phosphorene. *Nano Lett* **2014,** *14* (10), 5733-9.
4. Liu, H.; Neal, A. T.; Zhu, Z.; Luo, Z.; Xu, X.; Tomanek, D.; Ye, P. D., Phosphorene: an unexplored 2D semiconductor with a high hole mobility. *ACS Nano* **2014,** *8* (4), 4033-41.
5. Liu, H.; Du, Y.; Deng, Y.; Ye, P. D., Semiconducting black phosphorus: synthesis, transport properties and electronic applications. *Chem Soc Rev* **2015,** *44* (9), 2732-43.
6. Wang, X.; Jones, A. M.; Seyler, K. L.; Tran, V.; Jia, Y.; Zhao, H.; Wang, H.; Yang, L.; Xu, X.; Xia, F., Highly anisotropic and robust excitons in monolayer black phosphorus. *Nature Nanotechnology* **2015,** *10*, 517.

7. Favron, A.; Gaufrès, E.; Fossard, F.; Phaneuf-L'Heureux, A.-L.; Tang, N. Y. W.; Lévesque, P. L.; Loiseau, A.; Leonelli, R.; Francoeur, S.; Martel, R., Photooxidation and quantum confinement effects in exfoliated black phosphorus. *Nature materials* **2015,** *14*, 826.
8. Luo, Z.; Maassen, J.; Deng, Y.; Du, Y.; Garrelts, R. P.; Lundstrom, M. S.; Ye, P. D.; Xu, X., Anisotropic in-plane thermal conductivity observed in few-layer black phosphorus. *Nature Communications* **2015,** *6*, 8572.
9. Doganov, R. A.; O'Farrell, E. C. T.; Koenig, S. P.; Yeo, Y.; Ziletti, A.; Carvalho, A.; Campbell, D. K.; Coker, D. F.; Watanabe, K.; Taniguchi, T.; Neto, A. H. C.; Özyilmaz, B., Transport properties of pristine few-layer black phosphorus by van der Waals passivation in an inert atmosphere. *Nature Communications* **2015,** *6*, 6647.
10. Zhang, L.; Hao, Y., Electronic and optical responses of quasi-one-dimensional phosphorene nanoribbons to strain and electric field. *Sci Rep-Uk* **2018,** *8* (1), 6089.
11. Miao, X. C.; Zhang, G. W.; Wang, F. J.; Yan, H. G.; Ji, M. B., Layer-Dependent Ultrafast Carrier and Coherent Phonon Dynamics in Black Phosphorus. *Nano Letters* **2018,** *18* (5), 3053-3059.
12. Kim, J.; Baik, S. S.; Ryu, S. H.; Sohn, Y.; Park, S.; Park, B.-G.; Denlinger, J.; Yi, Y.; Choi, H. J.; Kim, K. S., Observation of tunable band gap and anisotropic Dirac semimetal state in black phosphorus. *Science* **2015,** *349* (6249), 723-726.
13. Bridgman, P. W., Two New Modifications of Phosphorus. *J Am Chem Soc* **1914,** *36* (7), 1344-1363.
14. Brent, J. R.; Savjani, N.; Lewis, E. A.; Haigh, S. J.; Lewis, D. J.; O'Brien, P., Production of few-layer phosphorene by liquid exfoliation of black phosphorus. *Chem Commun* **2014,** *50* (87), 13338-13341.
15. Hanlon, D.; Backes, C.; Doherty, E.; Cucinotta, C. S.; Berner, N. C.; Boland, C.; Lee, K.; Harvey, A.; Lynch, P.; Gholamvand, Z.; Zhang, S.; Wang, K.; Moynihan, G.; Pokle, A.; Ramasse, Q. M.; McEvoy, N.; Blau, W. J.; Wang, J.; Abellan, G.; Hauke, F.; Hirsch, A.; Sanvito, S.; O'Regan, D. D.; Duesberg, G. S.; Nicolosi, V.; Coleman, J. N., Liquid exfoliation of solvent-stabilized few-layer black phosphorus for applications beyond electronics. *Nature Communications* **2015,** *6*, 8563.
16. Buscema, M.; Groenendijk, D. J.; Steele, G. A.; van der Zant, H. S. J.; Castellanos-Gomez, A., Photovoltaic effect in few-layer black phosphorus PN junctions defined by local electrostatic gating. *Nature Communications* **2014,** *5*, 4651.
17. Deng, Y.; Luo, Z.; Conrad, N. J.; Liu, H.; Gong, Y.; Najmaei, S.; Ajayan, P. M.; Lou, J.; Xu, X.; Ye, P. D., Black phosphorus-monolayer MoS2 van der Waals heterojunction p-n diode. *Acs Nano* **2014,** *8* (8), 8292-9.
18. Li, L.; Yu, Y.; Ye, G. J.; Ge, Q.; Ou, X.; Wu, H.; Feng, D.; Chen, X. H.; Zhang, Y., Black phosphorus field-effect transistors. *Nature Nanotechnology* **2014,** *9*, 372.
19. Churchill, H. O. H.; Jarillo-Herrero, P., Phosphorus joins the family. *Nature Nanotechnology* **2014,** *9*, 330.
20. Buscema, M.; Groenendijk, D. J.; Blanter, S. I.; Steele, G. A.; van der Zant, H. S. J.; Castellanos-Gomez, A., Fast and Broadband Photoresponse of Few-Layer Black Phosphorus Field-Effect Transistors. *Nano Lett* **2014,** *14* (6), 3347-3352.
21. Yuan, H.; Liu, X.; Afshinmanesh, F.; Li, W.; Xu, G.; Sun, J.; Lian, B.; Curto, A. G.; Ye, G.; Hikita, Y.; Shen, Z.; Zhang, S.-C.; Chen, X.; Brongersma, M.; Hwang, H. Y.; Cui, Y., Polarization-sensitive broadband photodetector using a black phosphorus vertical p–n junction. *Nature Nanotechnology* **2015,** *10*, 707.
22. Youngblood, N.; Chen, C.; Koester, S. J.; Li, M., Waveguide-integrated black phosphorus photodetector with high responsivity and low dark current. *Nat Photonics* **2015,** *9*, 247.

23. Perello, D. J.; Chae, S. H.; Song, S.; Lee, Y. H., High-performance n-type black phosphorus transistors with type control via thickness and contact-metal engineering. *Nature Communications* **2015,** *6*, 7809.
24. Wang, L.; Xu, Q. C.; Xu, J.; Weng, J., Synthesis of hybrid nanocomposites of ZIF-8 with two-dimensional black phosphorus for photocatalysis. *Rsc Advances* **2016,** *6* (73), 69033-69039.
25. Shao, J.; Xie, H.; Huang, H.; Li, Z.; Sun, Z.; Xu, Y.; Xiao, Q.; Yu, X.-F.; Zhao, Y.; Zhang, H.; Wang, H.; Chu, P. K., Biodegradable black phosphorus-based nanospheres for in vivo photothermal cancer therapy. *Nature Communications* **2016,** *7*, 12967.
26. Tao, W.; Zhu, X. B.; Yu, X. H.; Zeng, X. W.; Xiao, Q. L.; Zhang, X. D.; Ji, X. Y.; Wang, X. S.; Shi, J. J.; Zhang, H.; Mei, L., Black Phosphorus Nanosheets as a Robust Delivery Platform for Cancer Theranostics. *Advanced Materials* **2017,** *29* (1).
27. Zheng, S. J.; Wu, E. X.; Feng, Z. H.; Zhang, R.; Xie, Y.; Yu, Y. Y.; Zhang, R.; Li, Q. N.; Liu, J.; Pang, W.; Zhang, H.; Zhang, D. H., Acoustically enhanced photodetection by a black phosphorus-MoS2 van der Waals heterojunction p-n diode. *Nanoscale* **2018,** *10* (21), 10148-10153.
28. Venuthurumilli, P. K.; Ye, P. D.; Xu, X. F., Plasmonic Resonance Enhanced Polarization-Sensitive Photodetection by Black Phosphorus in Near Infrared. *Acs Nano* **2018,** *12* (5), 4861-4867.
29. Liu, C. L.; Wang, L.; Chen, X. S.; Zhou, J.; Tang, W. W.; Guo, W. L.; Wang, J.; Lu, W., Top-gated black phosphorus phototransistor for sensitive broadband detection. *Nanoscale* **2018,** *10* (13), 5852-5858.
30. Gao, J. B.; Rao, A. M.; Li, H. B.; Zhang, J. B.; Chen, O., Carrier Transport Dynamics in High Speed Black Phosphorus Photodetectors. *Acs Photonics* **2018,** *5* (4), 1412-1417.
31. Yang, B. W.; Yin, J. H.; Chen, Y.; Pan, S. S.; Yao, H. L.; Gao, Y. S.; Shi, J. L., 2D-Black-Phosphorus-Reinforced 3D-Printed Scaffolds:A Stepwise Countermeasure for Osteosarcoma. *Advanced Materials* **2018,** *30* (10).
32. Li, C.; Wu, Y.; Deng, B. C.; Xie, Y. J.; Guo, Q. S.; Yuan, S. F.; Chen, X. L.; Bhuiyan, M.; Wu, Z. S.; Watanabe, K.; Taniguchi, T.; Wang, H. L.; Cha, J. J.; Snure, M.; Fei, Y. W.; Xia, F. N., Synthesis of Crystalline Black Phosphorus Thin Film on Sapphire. *Advanced Materials* **2018,** *30* (6).
33. Gao, G. Y.; Wan, B. S.; Liu, X. Q.; Sun, Q. J.; Yang, X. N.; Wang, L. F.; Pan, C. F.; Wang, Z. L., Tunable Tribotronic Dual-Gate Logic Devices Based on 2D MoS2 and Black Phosphorus. *Adv Mater* **2018,** *30* (13).
34. Xu, Z.-L.; Lin, S.; Onofrio, N.; Zhou, L.; Shi, F.; Lu, W.; Kang, K.; Zhang, Q.; Lau, S. P., Exceptional catalytic effects of black phosphorus quantum dots in shuttling-free lithium sulfur batteries. *Nature Communications* **2018,** *9* (1), 4164.
35. Tran, V.; Soklaski, R.; Liang, Y.; Yang, L., Layer-controlled band gap and anisotropic excitons in few-layer black phosphorus. *Phys Rev B* **2014,** *89* (23), 235319.
36. Jain, A.; McGaughey, A. J. H., Strongly anisotropic in-plane thermal transport in single-layer black phosphorene. *Sci Rep-Uk* **2015,** *5*, 8501.
37. Zhou, Y.; Zhang, M.; Guo, Z.; Miao, L.; Han, S.-T.; Wang, Z.; Zhang, X.; Zhang, H.; Peng, Z., Recent advances in black phosphorus-based photonics, electronics, sensors and energy devices. *Materials Horizons* **2017,** *4* (6), 997-1019.
38. Haghighat-Shishavan, S.; Nazarian-Samani, M.; Nazarian-Samani, M.; Roh, H. K.; Chung, K. Y.; Cho, B. W.; Kashani-Bozorg, S. F.; Kim, K. B., Strong, persistent superficial oxidation-assisted chemical bonding of black phosphorus with multiwall carbon nanotubes for high-capacity ultradurable storage of lithium and sodium. *Journal of Materials Chemistry A* **2018,** *6* (21), 10121-10134.

39. Bat-Erdene, M.; Batmunkh, M.; Tawfik, S. A.; Fronzi, M.; Ford, M. J.; Shearer, C. J.; Yu, L. P.; Dadkhah, M.; Gascooke, J. R.; Gibson, C. T.; Shapter, J. G., Efficiency Enhancement of Single-Walled Carbon Nanotube-Silicon Heterojunction Solar Cells Using Microwave-Exfoliated Few-Layer Black Phosphorus. *Advanced Functional Materials* **2017,** *27* (48).
40. Guo, Z.; Chen, S.; Wang, Z.; Yang, Z.; Liu, F.; Xu, Y.; Wang, J.; Yi, Y.; Zhang, H.; Liao, L.; Chu, P. K.; Yu, X.-F., Metal-Ion-Modified Black Phosphorus with Enhanced Stability and Transistor Performance. *Adv Mater* **2017,** *29* (42), 1703811.
41. Zhu, X.; Zhang, T.; Jiang, D.; Duan, H.; Sun, Z.; Zhang, M.; Jin, H.; Guan, R.; Liu, Y.; Chen, M.; Ji, H.; Du, P.; Yan, W.; Wei, S.; Lu, Y.; Yang, S., Stabilizing black phosphorus nanosheets via edge-selective bonding of sacrificial C60 molecules. *Nature Communications* **2018,** *9* (1), 4177.
42. Abate, Y.; Akinwande, D.; Gamage, S.; Wang, H.; Snure, M.; Poudel, N.; Cronin, S. B., Recent Progress on Stability and Passivation of Black Phosphorus. *Adv Mater* **2018,** *30* (29), 1704749.
43. Abellan, G.; Wild, S.; Lloret, V.; Scheuschner, N.; Gillen, R.; Mundloch, U.; Maultzsch, J.; Varela, M.; Hauke, F.; Hirsch, A., Fundamental Insights into the Degradation and Stabilization of Thin Layer Black Phosphorus. *J Am Chem Soc* **2017,** *139* (30), 10432-10440.
44. LeBeau, J. M.; Findlay, S. D.; Allen, L. J.; Stemmer, S., Quantitative Atomic Resolution Scanning Transmission Electron Microscopy. *Phys Rev Lett* **2008,** *100* (20), 206101.
45. Rosenauer, A.; Gries, K.; Müller, K.; Pretorius, A.; Schowalter, M.; Avramescu, A.; Engl, K.; Lutgen, S., Measurement of specimen thickness and composition in Al(x)Ga(1-x)N/GaN using high-angle annular dark field images. *Ultramicroscopy* **2009,** *109* (9), 1171-1182.
46. Lobato, I.; Van Dyck, D., MULTEM: A new multislice program to perform accurate and fast electron diffraction and imaging simulations using Graphics Processing Units with CUDA. *Ultramicroscopy* **2015,** *156*, 9-17.
47. Hernandez, Y.; Nicolosi, V.; Lotya, M.; Blighe, F. M.; Sun, Z.; De, S.; McGovern, I. T.; Holland, B.; Byrne, M.; Gun'Ko, Y. K.; Boland, J. J.; Niraj, P.; Duesberg, G.; Krishnamurthy, S.; Goodhue, R.; Hutchison, J.; Scardaci, V.; Ferrari, A. C.; Coleman, J. N., High-yield production of graphene by liquid-phase exfoliation of graphite. *Nat Nanotechnol* **2008,** *3* (9), 563-8.
48. Jones, L.; Yang, H.; Pennycook, T. J.; Marshall, M. S. J.; Van Aert, S.; Browning, N. D.; Castell, M. R.; Nellist, P. D., Smart Align-a new tool for robust non-rigid registration of scanning microscope data. *Adv Struct Chem Imag* **2015,** *1*.
49. Lucas, G.; Burdet, P.; Cantoni, M.; Hebert, C., Multivariate statistical analysis as a tool for the segmentation of 3D spectral data. *Micron* **2013,** *52-53*, 49-56.
50. Perdew, J. P.; Burke, K.; Ernzerhof, M., Generalized gradient approximation made simple. *Physical review letters* **1996,** *77* (18), 3865-3868.
51. Grimme, S.; Antony, J.; Ehrlich, S.; Krieg, H., A consistent and accurate ab initio parametrization of density functional dispersion correction (DFT-D) for the 94 elements H-Pu. *J Chem Phys* **2010,** *132* (15), 154104.
52. Henkelman, G.; Uberuaga, B. P.; Jonsson, H., A climbing image nudged elastic band method for finding saddle points and minimum energy paths. *Journal of Chemical Physics* **2000,** *113* (22), 9901-9904.
53. Henkelman, G.; Jonsson, H., Improved tangent estimate in the nudged elastic band method for finding minimum energy paths and saddle points. *Journal of Chemical Physics* **2000,** *113* (22), 9978-9985.

54. Ophus, C., A fast image simulation algorithm for scanning transmission electron microscopy. *Adv Struct Chem Imaging* **2017,** *3* (1), 13.
55. Using the Prismatic STEM image simulation tool.

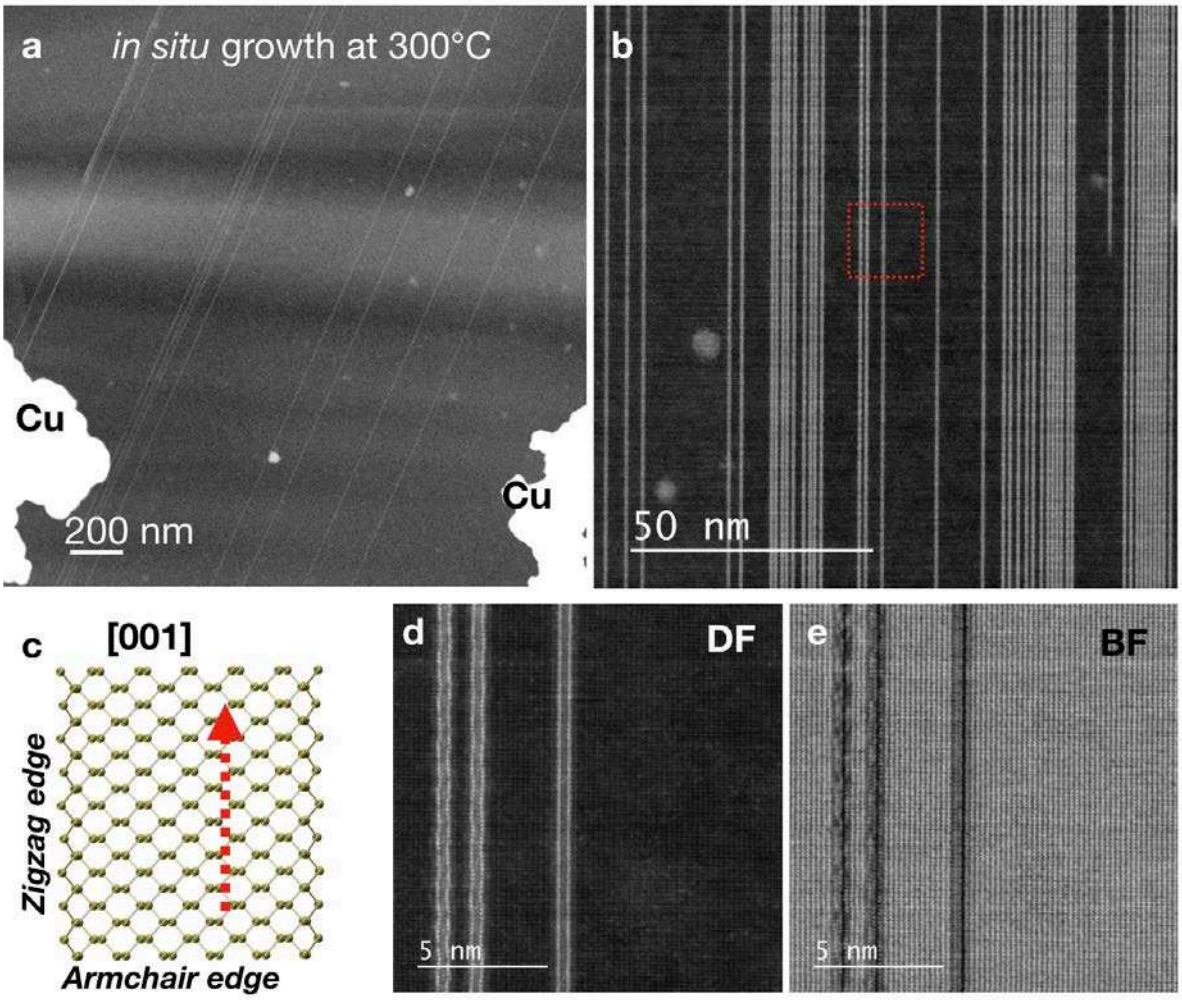

Figure 1: Rapid self-assembly of Copper (Cu) heterostructures of high aspect ratio templated by the Black Phosphorus (BP) lattice. ***a)*** *High-angle annular dark field (HAADF) Scanning Transmission Electron Microscopy (STEM) image of the heterostructures formed during in situ heating to 300 °C. The Cu heterostructures were found to form rapidly, with formation speed >100 nm/sec.* ***b)*** *Large arrays of parallel Cu heterostructures in the BP were found to self-assemble.* ***c)*** *Atomic model of a BP nanosheet viewed along the [001] crystallographic directions; the red arrow illustrates the direction of the Cu heterostructure growth.* ***d)*** *High resolution HAADF STEM image and* ***e)*** *corresponding Bright Field (BF)*

image of the same region as marked in red in b), showing a pair of undulating Cu lines and a third straighter line of Cu.

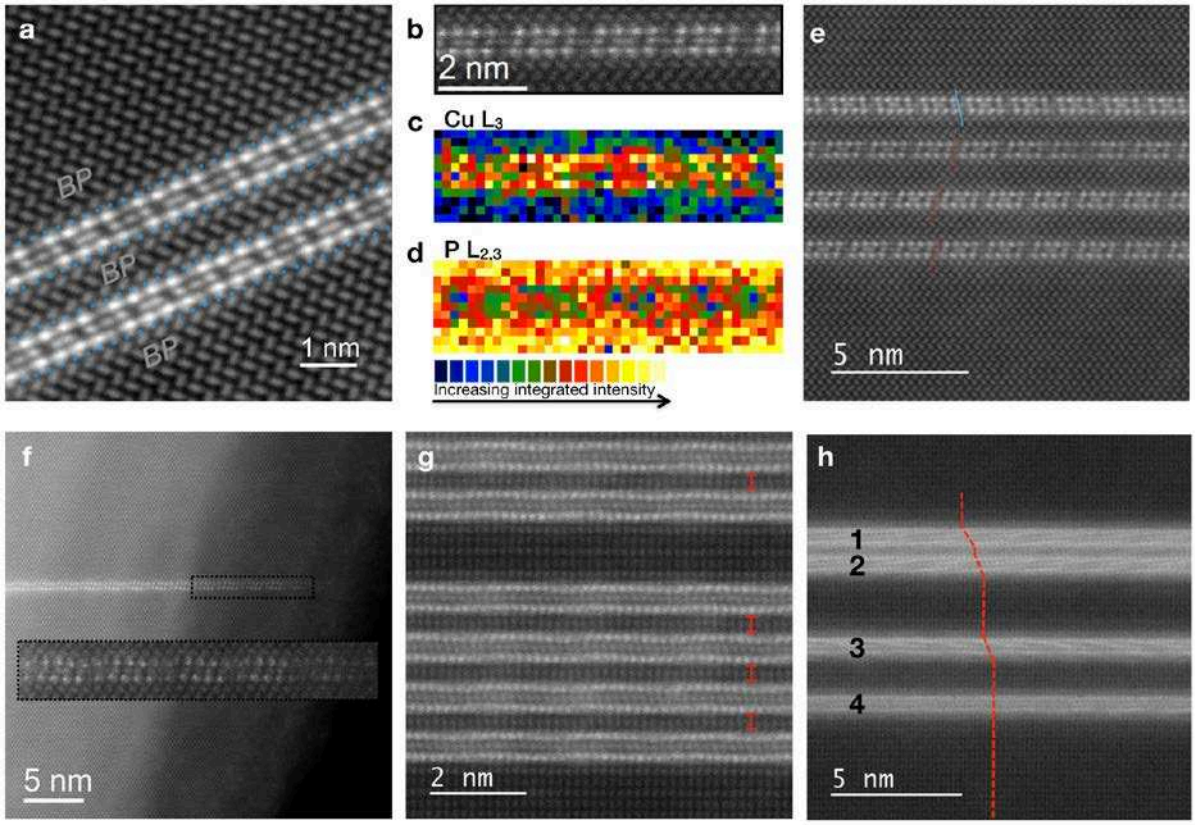

Figure 2: Three-atoms-wide polymorph chiral Copper (Cu) structures templated by Black Phosphorus (BP) nanosheets. *Orientations* ***a-e)*** R17/-R17 *and* ***f-h)*** *[001] revealed that the Cu structures are only 3-atoms-wide with* ***a)****** a sharp interface between Cu and phosphorus (marked with blue dotted line).* ***b)-d)*** *Compositional analysis (using CL EELS) confirmed that the structure is composed solely of Cu.* ***e)-h)*** *Polymorphisms and chirality: In the EM projections of the Cu in the BP, different stepping behavior was observed (dotted red line vs continuous blue line in* ***e)*** *and red line in* ***h)****).* ***f)*** *In the thinner BP sheets, the Cu structures exhibit undulations in the R17 orientation. Relative intensities of the Cu structures in thinner BP sheets (inset in f)) were different compared to the thicker BP nanosheets (in* ***e)****).* ***g)*** *Cu structures exhibit undulating patterns and were regularly spaced (red markings).* ***h)*** *The undulating pattern varied across the structures: 1,2 and 4 (where 4 only showed very faint undulating pattern) are of different chirality compared to 3. In the projections of the* R17/-R17 *orientation, the Cu structures appear to introduce a different step into the BP in regions*

*of same thickness. Structures 1-3 introduce a step, but 4 does not (red dotted line). (*Image was frame-averaged as described in [35].)*

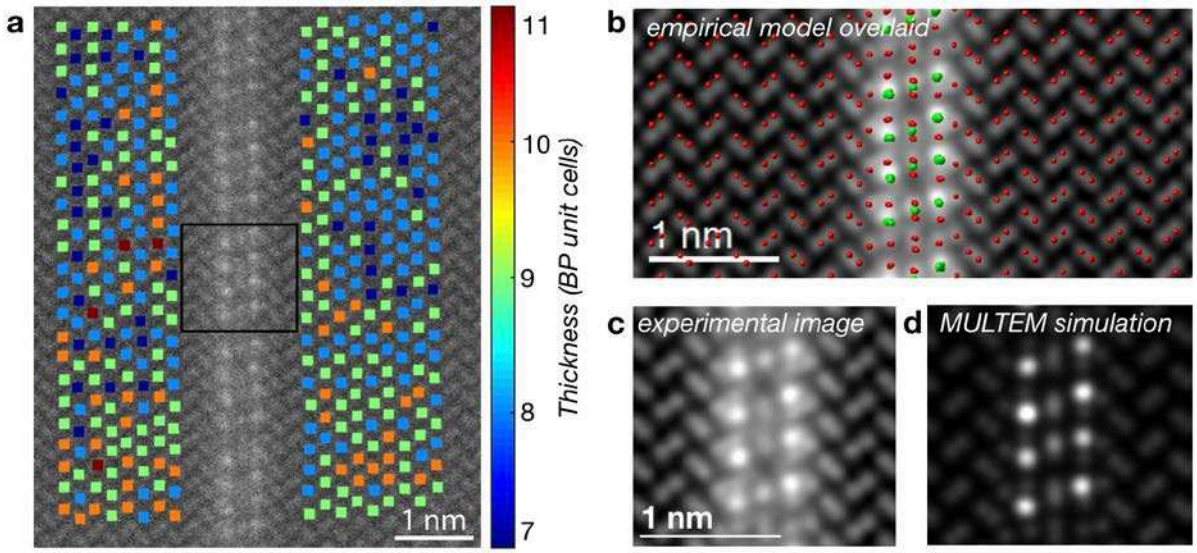

Figure 3: Thickness of copper (Cu) heterostructures in the BP determined using quantitative imaging. a) *The typical thickness of the BP nanosheets for Cu//BP hybrids (here in R17/-R17 orientation) was found to be 9 unit cells, or ~5.5 nm.* ***b)*** *Empirical model structure obtained to estimate thickness of the Cu in the BP lattice overlaid over template-matched experimental STEM image of Cu structures in BP nanosheets (experimental image alone in* ***c)*****). **d)** MULTEM simulated image obtained from the empirical model structure confirming that the Cu structures have a certain thickness. (*frame-averaged [35], then template-matched, then denoised.)*

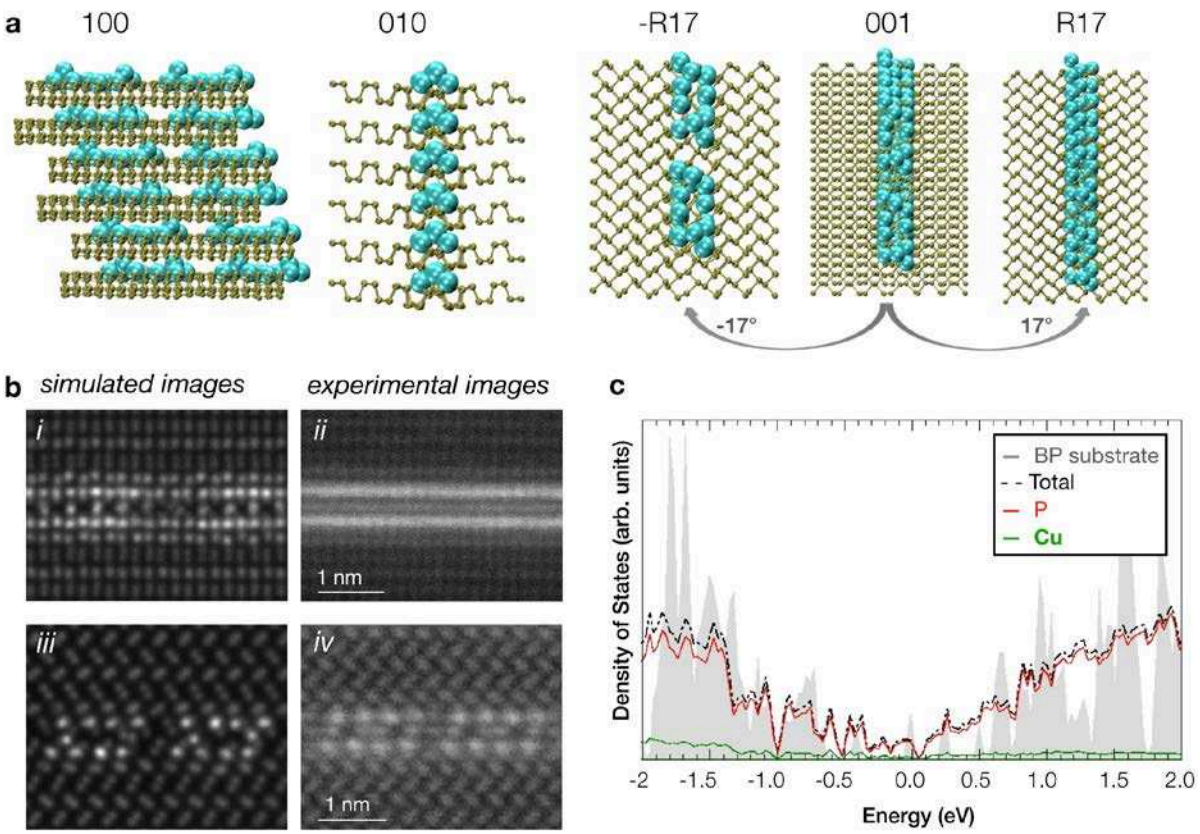

Figure 4: Theoretical investigation of chiral polymorphism and metallic nature. *Chiral, stable and energetically favorable Copper (Cu) heterostructures in the Black Phosphorus (BP) nanosheets found using an iterative combination of density functional theory (DFT), image simulation and comparison to experiment.* ***a)*** *Ball and stick representation of the structure that was found to provide the closest match with experiment in orientations [100], [010], -R17, [100] and R17. Green and cyan balls represent P and Cu atoms, respectively.* ***b)*** *Simulated images*[55] *of the structure shown in* ***i)*** *[001] orientation and* ***iii)*** *-R17 orientation and compared to experimental STEM images in the same orientation shown in* ***ii)*** *and* ***iv)*** *respectively.* ***c)*** *Density of states (DOS), of the structure as shown in* ***a)*** *represented with a dashed black line, suggests that the heterostructure in the BP nanosheet is metallic. DOS of the clean BP substrate and the Projected DOS on P and Cu atoms of the structure are also represented in red and green, respectively.*

The table of contents entry

A simple and reproducible method to trigger self-assembly of arrays of Cu heterostructures templated by the structural anisotropy in black phosphorus (BP) nanosheets is presented. Using multimodal electron microscopy techniques the Cu structures will be shown to be atomically-thin heterostructures. Using density functional theory calculations, the growth process, the atomic structure and metallic nature of the Cu heterostructures in BP were investigated.

Keyword heterostructures, black phosphorus, self-assembly, chiral, 2D materials, nanostructures

Hannah C. Nerl, Anuj Pokle, Lewys Jones, Knut Müller-Caspary, Karel H.W. van den Bos,Clive Downing, Eoin K. McCarthy, Nicolas Gauquelin, Quentin M. Ramasse, Ivan Lobato, Dermot Daly, Juan Carlos Idrobo, *Sandra Van Aert, Gustaaf Van Tendeloo, Stefano Sanvito, Jonathan N. Coleman, *Clotilde S. Cucinotta and *Valeria Nicolosi

Self-assembly of atomically-thin chiral Copper heterostructures templated by Black Phosphorus